14th International Symposium on Turbulence and Shear Flow Phenomena (TSFP14)
Heidelberg, Germany, July 28-31, 2026

EXPERIMENTAL COMPARISON OF DYNAMIC STALL ACROSS THREE DISTINCT AIRFOILS

Dylan T. Hilman
Department of Mechanical Engineering
University of Alberta
116 St & 85 Ave Edmonton, Alberta T6G 2R3, Canada
hilman@ualberta.ca

Sina Ghaemi
Department of Mechanical Engineering
University of Alberta
116 St & 85 Ave Edmonton, Alberta T6G 2R3, Canada
ghaemi@ualberta.ca

ABSTRACT

An experimental investigation on the development of dynamic stall using force and flow measurement is presented. Three finite wings were made from symmetric airfoils which exhibit distinct static stall behaviour known as trailing-edge stall, thin-airfoil stall, and leading-edge stall. Wings were analysed under dynamic conditions by pitching them about their quarter-chord in a wind tunnel at a Reynolds number of 260,000. Planar particle image velocimetry (PIV) was used alongside aerodynamic force measurement to evaluate criteria which quantitatively identify the transition between stages of dynamic stall. It was found that the sequence of dynamic stall was qualitatively consistent between airfoils. During pitch-up the wings experience delayed flow separation with an increased maximum lift at high angles of attack, followed by significant flow separation and large lift hysteresis during pitch down. However, the quantitative criteria commonly used to define the transition between the six stages of dynamic stall development: *attached flow*, *primary instability, vortex formation, stall onset, stall, and flow reattachment* occur in an inconsistent sequence between airfoils. Several metrics used to compare the severity of dynamic stall are investigated.

INTRODUCTION

Any lifting body that experiences a rapid increase in angle of attack (α) beyond their static stall angle (α_{ss}) experiences dynamic stall. The forces experienced during the dynamic stall cycle follow a large hysteresis curve due to the differences in flow structures and flow attachment during pitch up and pitch down motions. Dynamic stall increases the risk of structural failure through both long- and short-term mechanisms: repeated exposure to force hysteresis contributes to fatigue, while gust-induced events can generate extreme loads that may cause abrupt failure. As a result, dynamic stall limits the control, longevity, and maneuverability of rotorcraft, (Leishman 2006), fixed-wing aircraft, (Carr 1988), wind turbines, (Le Fouest and Mulleners 2022; Le Fouest et al. 2023), and drones (Gardner et al. 2023). The accuracy and effectiveness of models and control algorithms mitigating the effects of dynamic stall are highly dependent on the underlying flow characteristics which in turn are heavily influenced to the model geometry.

The overall description of dynamic stall development has often been qualitatively generalized across different airfoil geometries with a common sequence of developmental stages based on early investigations by Carr et al. (1977), McCroskey (1981), and Carr (1988). These stages were verified using flow-field structures identified via particle image velocimetry (PIV) by Mulleners and Raffel (2012) and provided event criteria for the transition between dynamic stall stages for a OA209 airfoil. Starting with the *attached flow stage*, and shortly followed by the *stall development stage*, the wing rapidly increases its α passed α_{ss}, flow reversal starts at the trailing edge and moves upstream. The *stall development stage,* which was further divided by Mulleners and Raffel (2013) and analysed further by Deparday and Mulleners (2019), is separated by the average height of clockwise vortices into the *primary instability stage* and *vortex formation stage*. The former covers the steady growth of shear layer, and the latter is characterized by an increase of the shear layer growth rate and the roll up of the shear layer forming the leading-edge vortex. The vortex increases lift significantly before its convection begins the *stall onset stage*. The maximum lift roughly correlates with the maximum of third POD mode of the flow field and was used by Mulleners and Raffel (2012) to identify the transition to the *stalled stage*. Here significant flow separation over the entire suction side of the airfoil and periodic vortex shedding causes fluctuating loading and a significant loss of lift. During pitch down the boundary layer reattaches from the leading edge toward the trailing edge in the final stage, *flow reattachment*, at sufficiently low α the aerodynamic loads return to their initial values seen in the *attached flow stage*.

The events detailed in Mulleners and Raffel (2012; 2013) were further connected to structures identified by an empirical modal decomposition in Ansel and Mulleners (2020) which also used the OA209 airfoil. Conversely, Ayancik and Mulleners (2022) compared the dynamic stall delay and post stall decay of three airfoils exhibiting similar static stall characteristics with increasing relative thickness, OA209, NACA0015, and NACA0018. Using a modified Goman-Khrabrov (G-K) method they succeeded in producing generalized physics-based time constants representative of the pre- and post-stall events. The effect of airfoil thickness on aerodynamic loads was also evaluated analytically in Motta et al. (2015) focusing on the attached region. Sharma and Visbal (2019) numerically compared the effect of airfoil thickness of four symmetric NACA airfoils and found the onset of dynamic stall was found to be marked by the bursting of a laminar separation bubble rather than the roll up of the shear layer. However, they did indicate the that the flow reversal region for the thickest airfoil may trigger dynamic stall, potentially blending classifications of stall type. However, its conclusions, as well as those by studies aimed at modelling and control, which utilized different airfoils, suggest that the geometry of the airfoil provides significant impact on dynamic stall and its resultant aerodynamic loading, which in turn, might be associated to the airfoil's static stall characteristics.

Broeren and Bragg (1998) investigated the effect of airfoil shape on the static lift force and separation mechanism across different airfoil shapes and identified three characteristic static stall types. Trailing-edge stall, where flow separation starts at the trailing edge and moves upstream causing gradual loss of lift. Thin-airfoil stall is a result of the formation, growth and collapse of a laminar separation bubble. Leading-edge stall has an abrupt flow separation from the leading edge and causes an immediate loss of lift. These distinct static behaviours are used to explore potential differences in dynamic stall development in the current investigation.

Using synchronized load measurements and flow visualization using planar PIV, the evolution of aerodynamic forces is correlated with quantified changes of the shear layer and variations in the development and convection of the leading-edge vortex. Through this comparison, we aim to determine how geometric differences effect the unsteady boundary-layer dynamics, vortex evolution, and hysteresis behaviour during dynamic stall.

EXPERIMENTAL METHODOLOGY

Experiments were conducted in the closed-loop wind tunnel at the University of Alberta with a test section with a cross-sectional area of 1.2×2.4 m^2. Tests were completed at a free-stream velocity of U_∞ = 15 m/s, corresponding to a chord-based Reynolds of 260,000.

Three symmetric airfoils were chosen for their distinct static stall characteristics at this Reynolds number based on the investigation from Broeren and Bragg (1998). The us1000root exhibits trailing-edge stall, the NACA64a010 which exhibits thin-airfoil stall, and the e472 exhibiting leading-edge stall referred to as TE stall/wing, TN stall/wing, and LE stall/wing, respectively. Wings were 3D printed using polylactic acid (PLA), with a chord of 0.3 m and span of 0.8 m, giving an aspect ratio of AR = 2.67. The surface was iteratively sanded up to 1000 grit sandpaper to ensure smoothness across the wing. After assembly, any gaps were filled with modelling clay and smoothed with a knife edge. As shown in figure 1 the pressure side of the wings were mounted on a streamlined sword connected to an actuating system which sat below the wind tunnel floor.

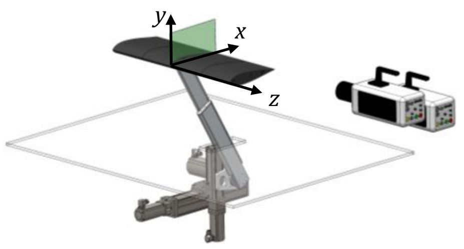

Figure 1. Experimental setup, with wing (TE shown), actuation system and planar PIV field of view

The custom-built dynamic actuation system consisted of three sub-units, an x-actuator moving in the streamwise axis, a y-actuator moving in the wall normal direction, and a rotational unit which rotates on the spanwise axis. Together this allowed three degree-of-freedom motion in the x-y plane with translation 300×100 mm^2 and rotation from -10° to 30° angle of attack. Actuators were powered with servo motors (Festo) with commands sent from a custom program (LabView, National Instruments) via EtherCAT cia402 protocol. During the measurements, the wings were sinusoidally oscillated around their quarter-chord about a mean angle α_0 = 16°, with an amplitude of α_1 = ±9°, and a reduced frequency $k = \pi f_{osc} c/U_\infty$ = 0.05 where f_{osc} = 0.8 Hz is the pitching frequency. Oscillation amplitude and frequency were chosen to produce a strong dynamic loading hysteresis for all three airfoils within the limits of the actuation system and load cell. The α was chosen for each airfoil to ensure the oscillation envelope captured both the fully attached and fully separated flow during the oscillation cycle.

Force measurement was sampled at 2,000 Hz using a 6-axis loadcell (ATI Mini-40), mounted inside the wing and recorded using a data acquisition system (National Instruments, 9620-05). Aerodynamic loading was isolated following procedures from Vicroy (2023). Phase-averaged wind off tests, containing only inertial data were subtracted from the raw wind-on tests, which contain both inertial and aerodynamic data. Loadcell data was synchronized with positioning images (Basler ace 2 Basic) captured at 50 Hz which identified wing orientation via optical markers on the wing tip.

The PIV measurement utilized two highspeed cameras (Photron S9) with Nikon lenses with a focal length f = 105 mm and a 2× teleconverter. A dual-cavity highspeed Nd: YLF laser (Litron LD-527) was used with cylindrical lenses to illuminate the regions of interest. Air was seeded using droplets dispersed by a fog generator. Planar PIV used a 1 mm thick laser sheet and saw cameras staggered to produce two 170×170 mm^2 overlapping fields of view with a 0.165 mm/pixel resolution.

Static wing tests consisted of 8,000 double-frame planar PIV images at 200 Hz over 40 seconds. For dynamic tests the acquisition frequency was increased to 260 Hz over 45 pitching cycles and repeated twice for each airfoil. Vector field calculation used a multi-pass ensemble of correlation for static tests with a final interrogation window of 12×12 pixel (1.98×1.98 mm^2). Dynamic tests used a standard double-frame correlation with a final interrogation window of 48×48 pixel (7.92×7.92 mm^2), (Davis 10.2.1, LaVision GmbH). All interrogation windows used a 75% overlap. Vectors with a difference of 2.5 times greater standard deviations from average were removed and replaced with interpolated vectors.

STATIC STALL ANALYSIS

Figure 2 shows the measured static lift coefficient near stall for all three wings. When following the red curve for the TE wing, increasing α shows a consistent slope until the maximum lift at 14° after which a moderate decrease in lift occurs. There is no indication of static hysteresis for this wing. The flow measurement with normalized streamwise velocity contours is shown in figure 3. The TE wing in figure 3a shows flow separation clearly initiating from the trailing edge. In contrast, the TN wing shown in green in figure 2 sees a larger reduction in lift slope before its maximum lift at α = 15°. Increasing α further results a brief reduction in lift before its value stabilizes to 0.65. In Broeren and Bragg (1998) at high angles of attack the lift for TN stall was observed to increase linearly in this region. In this experiment, this increase is not significant, most likely due to the three-dimensionality of the wing promoting flow separation at the wing tips. Additionally, the TN airfoil develops a separation bubble that reattaches about 0.5C at an angle of attack of 11°, as seen in figure 3b. Finally, at 17° the LE airfoil sees the relatively largest maximum static lift, shown in blue in figure 2. The LE wing is the only one to have a strong static lift hysteresis, after flow separation occurs the lift maintains a value of 0.6 during downstroke rather than following the values during upstroke. Before stall, the TE wing flow shown in figure 3c maintains attachment rather than showing moderate flow separation as the other wings did. The aerodynamic flow field measurements and loading in figures 2 and 3 are consistent with the results of Broeren and Bragg (1998), confirming distinct static stall mechanisms among the airfoils and providing a basis for extending the analysis to the dynamic regime.

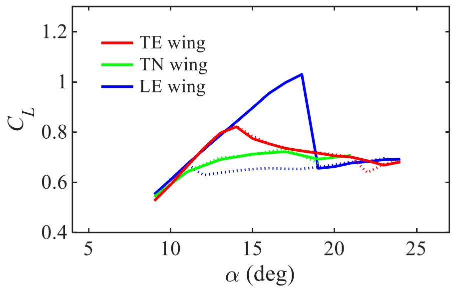

Figure 2. Static lift coefficient for all three wings, solid line indicates increasing α, dotted line indicates a decreasing α.

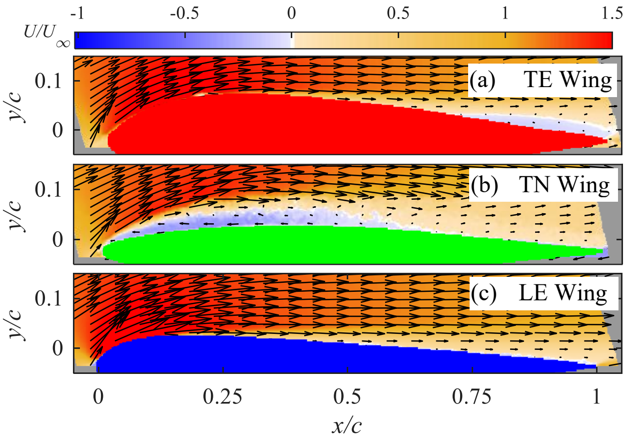

Figure 3. Planar measurement of the flow just before maximum lift for static stall, (a) TE wing at $\alpha = 14°$, (b) TN wing at $\alpha = 11°$, and (c) LE wing at $\alpha = 16°$

DYNAMIC STALL ANALYSIS

The airfoils in this study were evaluated using the same stages and transitional criteria as in Mulleners and Raffel (2012; 2013). As in their work, we again focus on the identification and characterization of the mechanisms of the flow development prior, during and after dynamic stall with markers indicating important events. The phase-averaged, quarter-chord lift and pitching moment coefficient are shown in C_L *vs.* α and C_M *vs.* α plots shown in figures 4 and 5, respectively. The phase averaged shear layer height, Δy, is determined by calculating average height of clockwise vortices above the airfoil surface such as those seen in figure 6. Regions of vorticity were identified using the Q-criterion with vortex centres being located using "regionprops" (MATLAB). In figure 6 the flow field corresponding to $C_{L,max}$ is illustrated for each airfoil with vortices shown in light blue and orange for clockwise and counterclockwise rotation respectively. The angle of attack at which the change in slope of the shear layer coincides with the maximum lift in Mulleners and Raffel (2013). For airfoils in this study the point of maximum lift and change in the shear layer slope did not coincide and are marked with separate points. The resulting Δy is used to differentiate stages of shear layer growth in figures 7a, 7c, and 7e. Proper orthogonal decomposition (POD) is used to quantify the development of dynamic stall in Mulleners and Raffel (2012) to decompose the flow fields into orthogonal spatial and temporal modes and sorts them by the relative energy of each mode. Two-dimensional flow $\mathbf{U} = (U, V)$ is decomposed using the method of snapshots as shown in equation 1.

$$\mathbf{U}(x,y,t) = \sum_{i=1}^{N} a_i(t)\,\psi_i(x,y) \qquad (1)$$

Here $a_i(t)$ is the temporal mode, which describes the relative energy contributed by the spatial mode, ψ, at a given time. POD was performed for each airfoil over their full data set. The normalized-phase-averaged temporal coefficient for the first three dominant modes relating to flow attachment, separation, and vortex development are shown for each wing in figures 7b, 7d, and 7f. All figures have the event indicators overlayed for comparison. The dynamic data shown comes from sinusoidal oscillations with $\alpha_0 = 16°$, $\alpha_1 = \pm 9°$ $k = 0.05$.

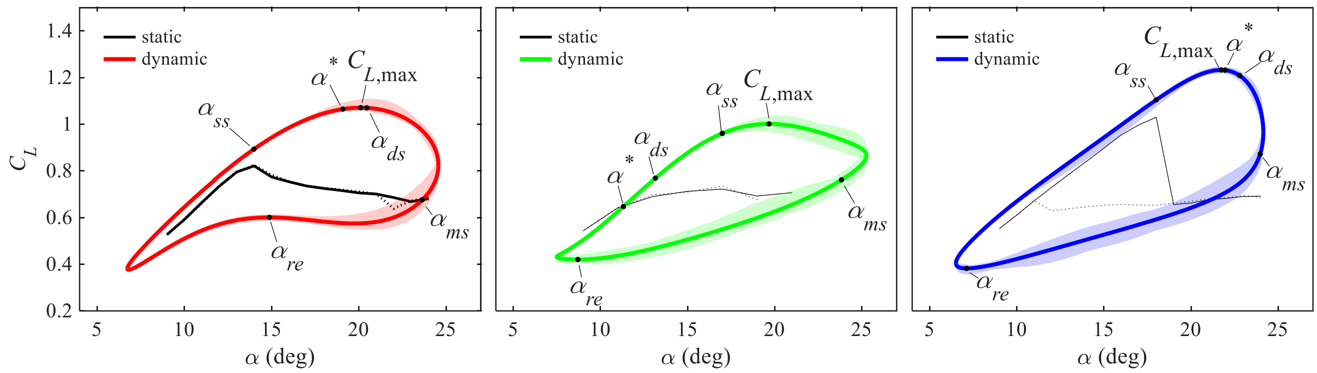

(a) TE Wing (b) LN Wing (c) LE Wing

Figure 4. Lift coefficient during stall for static and dynamic tests with key events during dynamic stall cycle indicated for a) TE wing, b) TN wing, c) LE wing. Dynamic test shown is f_{osc} = 0.8 Hz, k = 0.05, α_1 = ±9. Solid black lines indicate static upstroke; dashed black indicate downstroke. Solid coloured lines represent phase-averaged dynamic data with the max-min envelope shown in shaded region

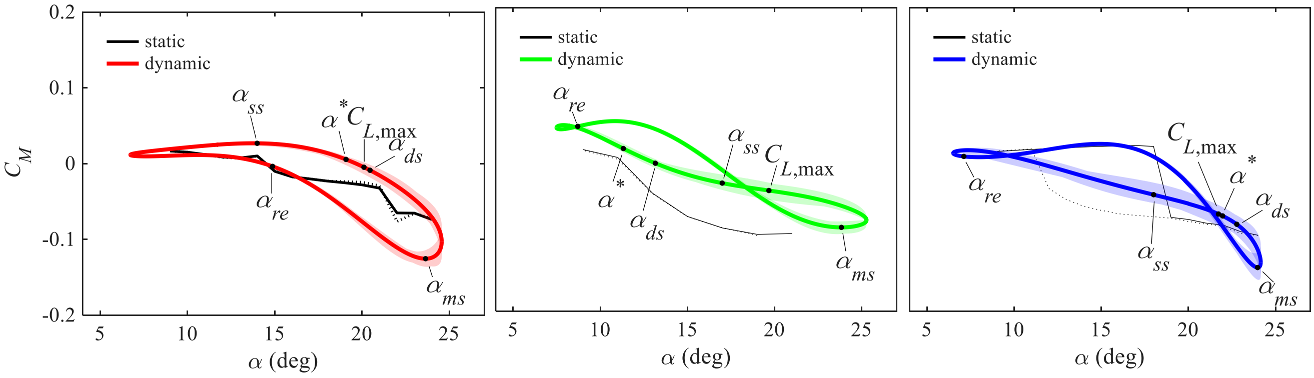

(a) TE Wing (b) LN Wing (c) LE Wing

Figure 5. Moment coefficient during stall for static and dynamic tests with key events during dynamic stall cycle indicated for a) TE wing, b) TN wing, c) LE wing. Dynamic test shown is f_{osc} = 0.8 Hz, k = 0.05, α_1 = ±9. Solid black lines indicate static upstroke; dashed black indicate downstroke. Solid coloured lines represent phase-averaged dynamic data with the max-min envelope shown in shaded region

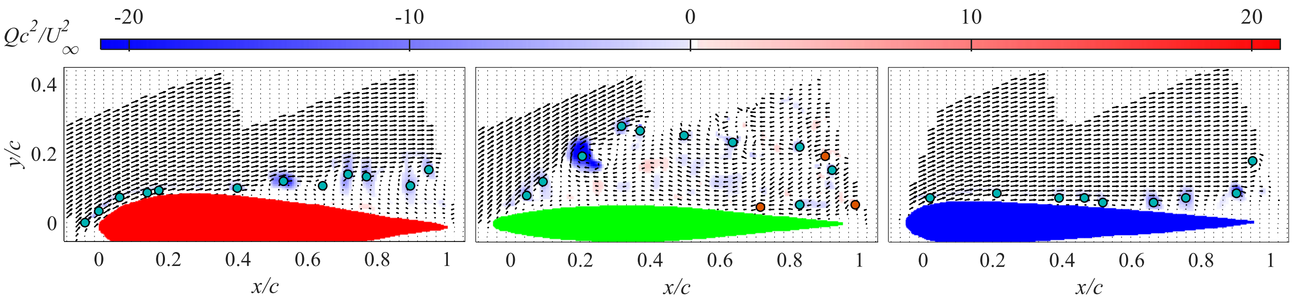

(a) TE Wing (b) LN Wing (c) LE Wing

Figure 6. Planar PIV measurement at $\alpha = C_{L,max}$ with vorticies identified using Q-criterion, clockwise highlighted with blue, and counter-clockwise vorticies in orange for (a) TE wing, α = 20.5° (b) TN wing, α = 19.7° (c) LE wing, α = 22.7°

Trailing-edge separation

The TE wing is used as a baseline since several previous dynamic stall investigations used the OA209 airfoil which, although being cambered, also exhibits trailing-edge stall characteristics. Starting from the attached flow stage where $\alpha = \alpha_{ss}$ and increasing the airfoil's angle of attack passed α_{ss}, the flow over the airfoil enters the *primary instability* stage. During this period, as seen in figure 7a the average height of clockwise vortices has increased as separation starts from the trailing edge, moving upstream. The end of the *primary instability* stage is marked with a change in the slope of the shear layer height, $\alpha = \alpha^*$, marking the start of the *vortex formation* stage. In previous studies this point also marked the maximum lift, for the TE wing there is a delay from the transition point until the $C_{L,max}$ occurs. Here, the shear layer height is increasing at a much greater rate, and flow has begun to detach closer to the leading edge. Clockwise vortices roll up along the surface of the airfoil and are recirculated into a larger structure forming the large stall vortex near the quarter-chord. After the lift begins to decrease the leading-edge vortex convects with the flow, $\alpha = \alpha_{ds}$, indicated by the maximum of the temporal coefficient corresponding to the third mode, shown in figure 7b, initiating the *stalled* stage. The shear layer height begins to fluctuate rapidly, lift begins reducing, and flow is separated from the entirety of the wing. The pitching moment continues to increase until its maximum at, $\alpha = \alpha_{ms}$, and does not noticeably correspond to any of the previously mentioned parameters. During the stalled staged there is periodic vortex shedding from the leading edge. During the onset of the *stalled* stage the first and second POD see an opposing change in their amplitude which gradually returns to pre-stall values as α reduces. The *stalled* stage ends once the lift begins to increase again, this is seen with reattachment starting from the leading edge towards the trailing edge in $\alpha = \alpha_{re}$. The shear layer height has not yet returned to pre-stall levels but is marked by an inflection point. For the TE wing this lift recovery begins before the end of the pitching cycle.

Thin airfoil separation

The dynamic stall development of the TN airfoil differs significantly from the TE wing and previous studies. The growth of the laminar separation bubble produces a unique lift curve shown in figure 4b; during the initial pitch up between 7° and 12° the curvature of the lift is convex and lower than static values. However, the lift slope is still positive, likely due to the extra lift generated from the recirculation that is generated before $\alpha = \alpha^*$. At these lower angles vortices still extend above the airfoil surface, raising the shear layer height much earlier in the cycle. Because of this, the indicators used for transitioning between stages are out of order compared to the baseline case. Between $\alpha = \alpha^*$ and $\alpha = \alpha_{ds}$ we see a shift in the separation point from the trailing edge past 0.5c toward the leading edge.

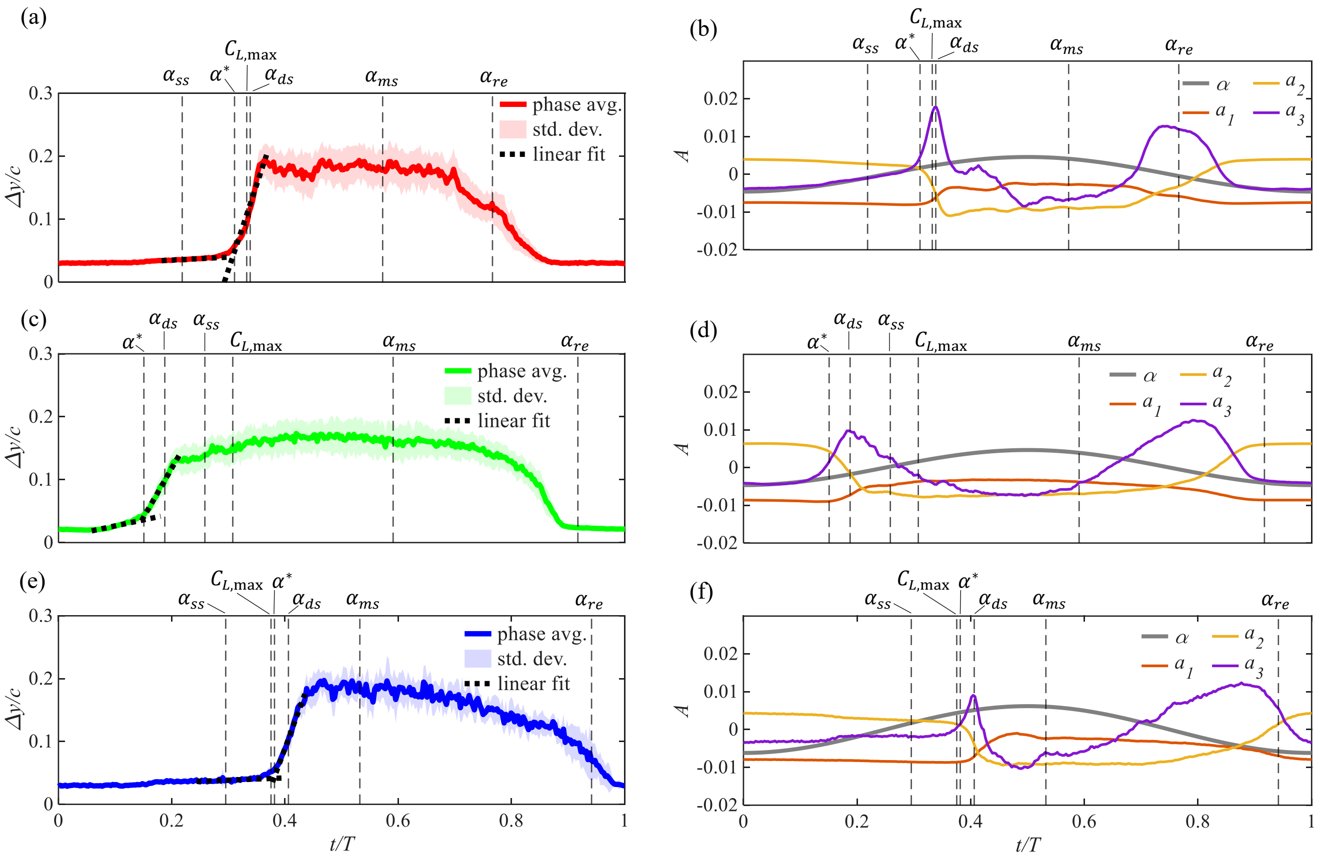

Figure 7. (a; c; e) Average shear layer height, Δy, and (b; d; f) first three modes of POD temporal coefficienct over an oscillation period with event criteria noted for (a; b) TE wing, (c; d) TN wing, and (e; f) LE wing

Flow near the trailing-edge attempts to reattach rather than separate as it did in the TE wing. The indicator for the vortex separation α_{ds} comes much earlier than any reduction in lift. The 3rd POD mode in figure 7d does see a local maximum, but unlike the TE wing which saw a prominent peak, the TN wing sees a gradual reduction in amplitude, as the vortex gradually loses coherance, rather than shedding away quickly. The temporal coefficient for mode 1, corresponding to flow separation has weakly increased, suggesting that the flow separated mode does not significantly dominate the flow, potentially supporting the fact lift is still increasing until 30% of the pitching cycle is completed. The flow field from α_{ds} to α_{ss} is separated and recirculating as the lift slope begins to reduce. While passing α_{ss} the moment inverts from a pitch up to pitch down. After the maximum lift a relatively moderate lift stall is seen with a consistant shear layer height. Lift does not recover until after mode 1 reduces, mode 2 increases and the shear layer in figure 7c reverts back to its initial height. Overall the TN wing acts as an exception to the typical evolution of dynamic stall, generating vortical structures early in the pitching cycle but maintaining recirculation over a greater period of time. It proves more resistant to the sharp peaks in loading and transient flow separation traditionally observed during dynamic stall.

LEADING-EDGE SEPARATION

The LE wing more closely resembles the quantified dynamic stall development from previous studies. Attached flow is maintained until α approaches α_{ss}. After this moment the flow has begun to separate from the trailing edge, with the separation point moving upstream and the shear layer height slowly increasing as seen in figure 7e. The transition from the *primary instability* to *vortex growth* stage also coincides with the maximum lift occurring around 22°. A relatively sharp loss in lift occurs and results in the roll up of the shear layer vortices. The leading-edge vortex is quickly formed and shed as indicated by the third temporal POD mode in figure 7f and shortly after the shear layer height stops increasing and instead fluctuates into the *stalled* stage. Here the shear layer height reaches a maximum approximately at the same time the peak moment occurs. It then gradually declines rather than maintaining its value like the TE and TN wings. Like the TN airfoil, the lift recovers very late in the oscillation cycle, but unlike the TN airfoil it recovers before the first and second modes, and the shear layer height returns to pre-stall values.

Severity of Dynamic Stall

The relative strength of dynamic stall can be determined by comparing the difference in lift during pitch up and pitch down. The severity of stall within an airfoil geometry has been categorized as "deep" or "light" based on the timing of α_{ds} occurring before or after the oscillation direction reverses, α_{rev}, respectively (Mulleners and Raffel, 2012). For individual airfoils this metric is helpful in determining the severity of stall and is also correlated to the normalized instantaneous effective unsteadiness $\dot{\alpha}_{ss} c/U_\infty$ (Mulleners and Raffel, 2013). Previous studies have observed that a larger $\dot{\alpha}_{ss} c/U_\infty$ results in earlier vortex development and deeper stall. A comparison of the lift curve area metric or area of hysteresis $A_{hys} = \oint C_L d\alpha \,/\, \Delta\alpha$, the timing of stall onset $\alpha_{rev} - \alpha_{ds}$, and the effected unsteadiness is shown in table 1.

Table 1. Dynamic stall severity

Airfoil	A_{hys}	$\alpha_{rev} - \alpha_{ds}$	$\dot{\alpha}_{ss}c/U_\infty$
TE wing	0.30	4.1°	0.0413
TN wing	0.27	11.8°	0.0408
LE wing	0.38	1.2°	0.0395

Based on the information contained in table 1, as well as seen visually in figure 4, the relative difference in lift from pitch up vs pitch down is greatest in the TE wing, and weakest in the TN wing. However, the indicator for the onset of dynamic stall shows an opposite relationship, while the effective unsteadiness results in roughly the same value. This presents a challenge when trying to compare the dynamic stall of airfoils with different stall types as current metrics are inadequate to describe the differences in stall severity. More analysis is required before generalization of the quantification of the dynamic stall process.

CONCLUSION

The dynamic stall development for three wings with distinct static stall characteristics were analysed and compared using a combination of load and PIV measurements. It was verified that the three wings presented static trailing-edge, thin-airfoil (bubble bursting), and leading-edge stall as categorized in Broeren and Bragg (1998). The evolution of dynamic stall was evaluated following procedure from Mulleners and Raffel (2012; 2013) to determine notable quantifiable events during an oscillation cycle. The unsteady flow development used six key events for comparison: the point at which the static stall angle was exceeded, the transition between *shear layer growth* and *vortex formation* indicated by the change in the rate of shear layer height, the maximum dynamic lift coefficient, the transition into the *stalled stage* indicated by the maximum of the third temporal POD mode, the maximum pitch moment, and reattachment, where lift begins to increase. It was found that the previously mentioned sequence of steps was generally consistent with the TE and LE wings, with small variations between the maximum lift, α^*, and α_{ds}. In contrast, the TN wing saw events occur in a significantly different order with vortex development beginning much earlier than the critical static stall angle. This was attributed to the formation of the laminar separation bubble, causing changes in the curvature of the lift coefficient and maintaining stability of the large recirculation region above the surface of the airfoil. This discrepancy in event sequence across airfoils requires careful consideration in models that use these indicators to predict the onset of dynamic stall. The severity of dynamic stall was also compared between the airfoil geometries and found that the LE wing had the “deepest” stall of the three airfoils tested while the TN had the “lightest” stall. This contradicted metrics used in previous studies which aimed to use generalized parameters to describe the effects of dynamic stall. Further work is required to develop generalized models for the effects of dynamic stall across different geometries with different stall types. This study demonstrates quantifiable events do commonly exist within the dynamic stall cycle for different airfoils. However, these cannot be used to universally characterize the sequence of dynamic stall development as they are dependent on the distinct stall mechanism. As a result, predictive models and control strategies must account for the individual airfoil behaviour to achieve reliable performance to predict and control aerodynamic loading during dynamic stall.

REFERENCES

Ayancik, F., & Mulleners, K., 2022, “All you need is time to generalise the Goman–Khrabrov dynamic stall model.” *Journal of Fluid Mechanics*, *942*, R8.

Broeren, A., & Bragg, M., 1998, “Low-frequency flowfield unsteadiness during airfoil stall and the influence of stall type”. *16th AIAA Applied Aerodynamics Conference*. 16th AIAA Applied Aerodynamics Conference.

Carr, L. W., 1988, “Progress in analysis and prediction of dynamic stall”. *Journal of Aircraft*, *25*(1), 6–17.

Carr, L. W., Mcalister, K. W., & Mccroskey, W. J., 1977, “Analysis of the development of dynamic stall based on oscillating airfoil experiments”. *NTRS.* (A-6674).

Deparday, J., & Mulleners, K., 2019, “Critical evolution of leading edge suction during dynamic stall”. *Journal of Physics: Conference Series*, *1037*, 022017.

Gardner, A. D., Jones, A. R., Mulleners, K., Naughton, J. W., & Smith, M. J., 2023, “Review of rotating wing dynamic stall: Experiments and flow control”. *Progress in Aerospace Sciences*, *137*, 100887.

Le Fouest, S., Fernex, D., & Mulleners, K., 2023, “Time scales of dynamic stall development on a vertical-axis wind turbine blade”. *Flow*, *3*, E11

Le Fouest, S., & Mulleners, K., 2022, “The dynamic stall dilemma for vertical-axis wind turbines”. *Renewable Energy*, *198*, 505–520.

Leishman, J. G., 2006, *Principles of helicopter aerodynamics*. Cambridge; New York: Cambridge University Press.

Mccroskey, W. J., 1981, “The phenomenon of dynamic stall”. *NTRS* (A-8464; Issue A-8464).

Motta, V., Guardone, A., & Quaranta, G., 2015, “Influence of airfoil thickness on unsteady aerodynamic loads on pitching airfoils”. *Journal of Fluid Mechanics*, *774*, 460–487.

Mulleners, K., & Raffel, M., 2012, “The onset of dynamic stall revisited”. *Experiments in Fluids*, *52*(3), Article 3.

Mulleners, K., & Raffel, M., 2013, “Dynamic stall development”. *Experiments in Fluids*, *54*(2), 1469.

Sharma, A., & Visbal, M., 2019, “Numerical investigation of the effect of airfoil thickness on onset of dynamic stall”. *Journal of Fluid Mechanics*, *870*, 870–900.

Vicroy, D. D., 2023, “A Guide to Forced Oscillation Data Processing and Analysis”. *NTRS*